Wave Motion 106 (2021) 102803

Contents lists available at ScienceDirect

Wave Motion

journal homepage: www.elsevier.com/locate/wamot

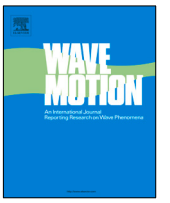

Spatio-temporal resolution improvement via weighted time-reversal

Manuel A. Jaimes *, Roel Snieder

Center for Wave Phenomena, Colorado School of Mines, 1500 Illinois Street, Golden, CO 80401, USA

ARTICLE INFO

Article history:
Received 24 October 2020
Received in revised form 15 July 2021
Accepted 17 July 2021
Available online 21 July 2021

Keywords:
Time-reversal
Resolution enhancement
Array optimization

ABSTRACT

We formulate resolution enhancement as a modified Backus–Gilbert inverse problem and determine the optimal complex weights that improve focusing of waves in space and time. The optimization corrects for receiver geometry. If we accurately know the location of a control point in the subsurface we can use the corresponding optimal weights to achieve enhanced focusing in a prescribed target zone surrounding the control point. Errors in the back propagation velocity and noisy data degrade the quality of focusing. The optimal wave field shows a blow-up behavior outside the optimization area. We show different measures of resolution to estimate the compression of the focal spot. The optimized weights amplify the high frequencies, but the algorithm also improves the focusing for monochromatic waves. At all frequencies our algorithm improves the resolution of the focal spot. We also show that for a uniformly sampled line array and a homogeneous medium, the weights used to enhance resolution have a negligible imaginary part and that they are oscillatory across the array used. To fully test the robustness of our algorithm, we also consider focusing in a heterogeneous medium with embedded scatterers and an irregular receiver line, and show that in this scenario we are also able to attain focusing improvement.

1. Introduction

Locating and imaging seismic sources has long been of interest in quantitative seismology and acoustics. Typically one uses the information contained in the wave motions caused by an earthquake to image that earthquake. Methods widely used to achieve source focusing include inverse scattering [1], phase conjugation [2], the inverse filter [3,4], time-reversal [5,6], and beam forming [7,8]. The latter two methods can be thought of as related processes [9–11]. In this paper we will mostly refer to time-reversal techniques but relevant analogies can be made to beam forming techniques. Further, we note that many other techniques in fields such as optics and wireless communications have been developed to enhance focusing. One technique that is useful as an analogy to the method we propose is spatial light modulation where one modifies the amplitude and phase of incident mono-chromatic waves to achieve spatial focusing upon propagation through an imaging system [12].

Seismologists often use time-reversal (TR) techniques for source focusing. Applications in seismology include analysis of earthquake source mechanisms and location estimation [13], monitoring of nuclear explosions and environmental applications [14], microseismic event location [15], reservoir monitoring [16], and reversed time migration [17]. Other

* Corresponding author.
E-mail address: mjaimescaballero@mymail.mines.edu (M.A. Jaimes).

https://doi.org/10.1016/j.wavemoti.2021.102803
0165-2125/

applications of TR techniques include underwater acoustics communication [18], three-dimensional elastic media communication [19], subsurface detection [20], study of electromagnetic waves [21], ultrasonic nondestructive testing [22], and real time tracking of gallstones during lithotripsy treatments [23].

TR techniques, as first developed by Parvulescu and Clay [5] and then expanded by Fink [6], rely on the even order of the time differential operator in the wave equation and on spatial reciprocity [24,25], and are valid both in homogeneous and inhomogeneous media [26,27]. As a result, it is possible to reverse the direction of time without altering the governing wave equation in non-dissipative environments [24]. This reversibility allows one to time-reverse data recorded at an array to estimate the location of sources. The time-reversal process consists of recording the physical signal at discrete receivers, time-reversing it, and sending back the time-reversed signal into the medium as a new source.

Optimally, the wave that one sends back to the medium should focus at the location where the event originated at time $t = 0$ provided one has an accurate knowledge of the velocity of the medium in which propagation takes place. However, even under ideal conditions, the focusing is spatially limited by the dominant wavelength of the wave field. This limit is the *wave diffraction limit*, which states that focusing cannot be achieved with a resolution better than half a wavelength $(\lambda/2)$ [28].

Francia [29] proposed the idea of imaging beyond the diffraction limit using optimal circular array apertures. However, this concept was not applicable at the time due to practical limitations regarding the large power required for the focusing. Recent tests in the optics community have shown that it is possible in practice to go beyond the diffraction limit to achieve *super-resolution*, which is of importance in the inverse source problem as well as conventional seismic imaging. Several seismological and non-seismological applications can benefit from the development of super-resolution techniques. These include the applications mentioned above but also other applications in which improving the resolution of the focusing at the source is desirable, such as focusing through human tissue [30], acoustic source reconstruction [31], localization of moving sound sources in shallow water [32], and focusing in turbid media [33]. New optical super-resolution technologies include Near-Field Scanning Optical Microscopy (SNOM) where a scanning array collects information of propagating and evanescent waves near the source, negative index super-lenses which allow transferring evanescent waves from the source to the image plane, and super-oscillatory imaging lenses which allow for imaging beyond the diffraction limit but often produce adjacent side-bands [34]. Several researchers in the field of acoustics have also developed novel super-resolution techniques. de Rosny and Fink [35] overcome the diffraction limit by combining a time reversal mirror with and an acoustic sink; Lerosey et al. [36] achieve super-resolution with far field time-reversal by placing random scatterers near the source location; Conti et al. [37] propose a near-field time-reversal approach which combines an acoustic sink with near field acoustic holography (NAH); Lemoult et al. [38] use acoustic resonators in the far field to achieve sub-wavelength resolution of sound; Mimani et al. [39] propose a sponge-layer time-reversal technique to improve aeroacoustic time-reversal imaging; and Mimani [40] propose an iterative version of the work by Mimani et al. [39]. In the seismological community Schuster et al. [41] introduce the idea of a seismic scanning tunneling macroscope, analogous to SNOM, which requires scatterers in the vicinity of the seismic source, a near-field technique. To overcome the near-field limitation, Guo et al. [42] show that in the far field it suffices to use resonant multiples in data migration to achieve sub-wavelength resolution. These developments, though insightful, depend on the presence of evanescent waves for near-field [41] or strongly scattered multiples for far-field [42].

To understand how we can attain enhanced resolution without evanescent waves or a strongly heterogeneous medium we pose the following question: Can we find frequency-dependent complex weights for each of the discrete receivers such that after time reversal, the focal spot at the source location resembles a delta function as closely as possible? We formulate this question as a modified Backus–Gilbert (BG) problem [43], in the sense that we search optimal weights that allow for reconstruction of a band-limited delta function in space and time, robust to errors in the velocity model and estimated source location. This is similar to weight optimization in beam forming where several authors have made use of BG techniques with the goal of focusing at a desired location [44–46]. Van Veen and Buckley [47] give an extensive discussion on widely used beam forming techniques. Note that in conventional beam forming one typically addresses spatial focusing (monochromatic pulses or narrow band data) whereas this paper addresses spatio-temporal focusing (polychromatic pulses or wide band data). Some research has been developed in the area of wide band beam forming [48–51] but more work remains to be done to attain an understanding of spatio-temporal focusing via beam forming [52]. Our approach is also linked to earlier work in the seismological community. Anderson et al. [53] achieve temporal focusing via deconvolution which is implemented as an inverse filter in the frequency domain. Bazargani and Snieder [54] minimize the difference between the backpropagated wave field and the time-reversed displacement field in the near source region by searching for optimal signals to send into the medium.

This paper is structured as follows: In Section 2 we formulate the optimal weights needed to achieve improved focusing. Next, in Section 3 we show the improvement of focusing in a standard seismic geometry when we use the optimal weights and estimate whether we obtain local or global focusing. We present a sensitivity analysis in Section 4 where we consider errors in source location and medium velocity, as well as noisy data. We illustrate different metrics of resolution in Section 5. Our results show not only the boosting of high frequencies but also the modulation of the source signal at all frequencies, which results in resolution improvement even for monochromatic waves. In Section 6 we show the frequency variation of the spectrum of the weights for four receiver locations along with the variation of the weights across the receiver array for different frequencies. We relate the spatial dependence of the weights along the receiver line to Tchebyscheff polynomials used in beam forming, and discuss how our algorithm is advantageous in the case of irregular arrays. In 7 we apply our method to focusing in a heterogeneous medium, and show how focusing is improved. We discuss the effectiveness of the optimal weights in time-reverse imaging in Section 8.

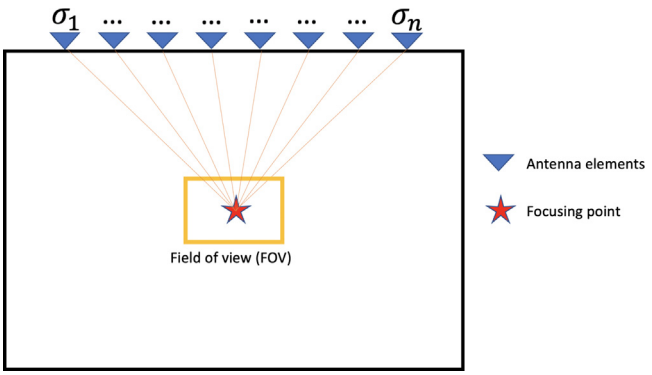

Fig. 1. Illustration of the TR experiment geometry for n receivers. We optimize focusing in a small area (FOV) around the source within the propagation medium. σ_i is the frequency dependent complex weight assigned to the ith receiver to optimize focusing.

2. Theory

Consider a source located at $\mathbf{x}_0$ which emits a pulse $S(t)$ at $t_0 = 0$. The time-reversal imaging operation in the time domain where the signal recorded by each receiver, $G(\mathbf{x}_i, t, \mathbf{x}_0) * S(t)$, is time reversed (i.e., $G(\mathbf{x}_i, \mathbf{x}_0, -t) * S(-t)$) and sent back into the medium from receiver i reads [55]

$$f_i(\mathbf{x}, \mathbf{x}_i, t) = G(\mathbf{x}, \mathbf{x}_i, t) * (G(\mathbf{x}_i, \mathbf{x}_0, -t) * S(-t)). \tag{1}$$

The index i specifies a particular receiver, the symbol "$*$" implies temporal convolution, and $\mathbf{x}$ specifies the location of the grid point in the field of view (FOV), see Fig. 1. $G(\mathbf{x}, \mathbf{x}_i, t)$ corresponds to the Green's function between receiver i and the location $\mathbf{x}$ in the FOV. Notice that although we use a focusing function which corresponds to unweighted time-reversal, one may use other focusing functions. Following Francia [29] and Rogers and Zheludev [34] we only optimize the focusing in the FOV.

We use the following convention for the Inverse Fourier Transform

$$f(t) = \int_{-\infty}^{+\infty} F(\omega) e^{-i\omega t} d\omega. \tag{2}$$

For a point impulsive source, assuming perfect sampling in space and time (i.e., a continuous cavity and infinite bandwidth), a full aperture (i.e, all possible illumination angles), and a wave field whose focusing is not diffraction limited, the time-reversal operation leads to perfect focusing, namely

$$\sum_i f_i(\mathbf{x}, \mathbf{x}_i, t) = \delta(\mathbf{x} - \mathbf{x}_0)\delta(t). \tag{3}$$

This corresponds in the frequency domain to

$$\sum_i F_i(\mathbf{x}, \mathbf{x}_i, \omega) = \delta(\mathbf{x} - \mathbf{x}_0). \tag{4}$$

Recall that Eq. (4) only holds for a wave field which is not diffraction-limited and that is fully sampled in space and time. In the real world we deal with imperfect sampling geometries and diffraction-limited focusing. In order to enhance focusing we use frequency-dependent complex weights σ_i which improve the localization of the time-reversed wave field, replacing Eq. (4) by

$$\sum_i \sigma_i(\mathbf{x}_i, \omega) F_i(\mathbf{x}, \mathbf{x}_i, \omega) = \delta(\mathbf{x} - \mathbf{x}_0). \tag{5}$$

Notice that we want to achieve spatial focusing for each frequency under consideration. To construct a delta function given a finite set of measurements we use a modified version of the Backus–Gilbert (BG) method [43], in which we minimize the following objective function for every angular frequency ω

$$J(\mathbf{x}, \mathbf{x}_0, \omega, \boldsymbol{\sigma}, \lambda) = \sum_i |\mathbf{x} - \mathbf{x}_0|^2 |\sigma_i(\mathbf{x}_i, \omega) F_i(\mathbf{x}, \mathbf{x}_i, \omega)|^2 + \lambda \left(\sum_i \sigma_i(\mathbf{x}_i, \omega) F_i(\mathbf{x}, \mathbf{x}_i, \omega) - \delta(\mathbf{x} - \mathbf{x}_0) \right). \tag{6}$$

We simultaneously minimize the objective function J at discrete points $\mathbf{x}$ in the FOV rather than minimizing the integral of J over FOV (as it is typically done in BG theory). This choice of minimization guarantees that we approach the desired

band-limited delta function in a point-wise fashion. We minimize this objective function in terms of the complex weights σ_i and a Lagrange multiplier λ. By minimizing the first term of Eq. (6) we force the energy of the weighted TR wave field to be zero at all points except at the source location. The second term forces the amplitude of the TR wave field to be non-zero at the source.

Next, we consider the partial derivatives of J with respect to the optimization parameters

$$\frac{\partial J}{\partial \sigma_i^*} = \sum_j |\mathbf{x} - \mathbf{x}_0|^2 \sigma_j(\mathbf{x}_j, \omega) F_j(\mathbf{x}, \mathbf{x}_j, \omega) F_i^*(\mathbf{x}, \mathbf{x}_i, \omega) + \lambda F_i^*(\mathbf{x}, \mathbf{x}_i, \omega), \tag{7}$$

$$\frac{\partial J}{\partial \lambda} = \sum_j \sigma_j(\mathbf{x}_j, \omega) F_j^*(\mathbf{x}, \mathbf{x}_j, \omega) - \delta(\mathbf{x} - \mathbf{x}_0), \tag{8}$$

here the superscript * implies complex conjugation. The subscripts i, j specify receivers from which the incident wave field is time-reversed.

To minimize the objective function we set the partial derivatives in Eqs. (7) and (8) equal to zero and solve this system of equations simultaneously for all grid points in FOV. These equations are written as

$$\underbrace{\begin{bmatrix} |\mathbf{x}_1 - \mathbf{x}_0|^2 F_1^1 F_1^{*1} & \cdots & |\mathbf{x}_1 - \mathbf{x}_0|^2 F_N^1 F_1^{*1} & F_1^{*1} \\ \vdots & \vdots & \vdots & \vdots \\ |\mathbf{x}_1 - \mathbf{x}_0|^2 F_1^1 F_N^{*1} & \cdots & |\mathbf{x}_1 - \mathbf{x}_0|^2 F_N^1 F_N^{*1} & F_N^{*1} \\ F_1^{*1} & \cdots & F_N^{*1} & 0 \\ \vdots & \vdots & \vdots & \vdots \\ |\mathbf{x}_k - \mathbf{x}_0|^2 F_1^k F_1^{*k} & \cdots & |\mathbf{x}_k - \mathbf{x}_0|^2 F_N^k F_1^{*k} & F_1^{*k} \\ \vdots & \vdots & \vdots & \vdots \\ |\mathbf{x}_k - \mathbf{x}_0|^2 F_1^k F_N^{*k} & \cdots & |\mathbf{x}_k - \mathbf{x}_0|^2 F_N^k F_N^{*k} & F_N^{*k} \\ F_1^{*k} & \cdots & F_N^{*k} & 0 \\ \vdots & \vdots & \vdots & \vdots \\ |\mathbf{x}_M - \mathbf{x}_0|^2 F_1^M F_1^{*M} & \cdots & |\mathbf{x}_M - \mathbf{x}_0|^2 F_N^M F_1^{*M} & F_1^{*M} \\ \vdots & \vdots & \vdots & \vdots \\ |\mathbf{x}_M - \mathbf{x}_0|^2 F_1^M F_N^{*M} & \cdots & |\mathbf{x}_M - \mathbf{x}_0|^2 F_N^M F_N^{*M} & F_N^{*M} \\ F_1^{*M} & \cdots & F_N^{*M} & 0 \end{bmatrix}}_{\boldsymbol{A}} \underbrace{\begin{bmatrix} \sigma_1 \\ \vdots \\ \sigma_N \\ \lambda \end{bmatrix}}_{\boldsymbol{\chi}} = \underbrace{\begin{bmatrix} 0 \\ \vdots \\ 1 \\ \vdots \\ 0 \\ \vdots \end{bmatrix}}_{\boldsymbol{b}}, \tag{9}$$

here $1 \leq k \leq M$, k is the grid point $\mathbf{x}$ in the field of view where we evaluate Eqs. (7) and (8), M is the number of grid points in the field of view, and N is the number of receivers. The superscript in F specifies the corresponding grid point whereas the subscript specifies the receiver number.

The only non-zero element in the vector on the right-hand side of Eq. (9) corresponds to setting $\mathbf{x} = \mathbf{x}_0$ in Eq. (8). Ultimately, we look for solutions to Eq. (9) that minimize $\|\mathbf{A}\boldsymbol{\chi} - \mathbf{b}\|$ in the least-squares sense. The solution vector $\boldsymbol{\chi}$ is found for each frequency independently, and contains the frequency-dependent complex weights σ_i and the Lagrange multiplier λ.

3. Focusing in homogeneous media

To simulate a typical seismic scenario, consider Fig. 1. This array illuminates the source at limited angles. We consider an array far away from the source (about 19 dominant wavelengths). Here we first consider a homogeneous acoustic medium. We perform the simulation and optimization using the Green's function $G^{2D}(\mathbf{r}, \mathbf{r}_0)$ which gives the outgoing wave solutions of the 2-D Helmholtz equation for our choice of Fourier transform convention,

$$G^{2D}(\mathbf{r}, \mathbf{r}_0) = \frac{-i}{4} H_0^1(k|\mathbf{r} - \mathbf{r}_0|),$$

where H_0^1 denotes the first Hankel function of degree zero [56]. We use 101 receivers, placed symmetrically above the source between -1000 and 1000 m, and located at a vertical distance of 1500 m from the source. For the FOV we use a box located from -50 to 50 m in the horizontal direction and 1450 to 1550 m in the vertical direction, with a grid spacing of 5 m in both directions. We use an acoustic medium with constant velocity $v = 1000$ m/s, frequency ranging from 0.32 Hz to 40 Hz with a spacing of 0.32 Hz, and a source wavelet with peak frequency of 12.73 Hz. Throughout this section and the rest of the paper we refer to pressure amplitude as amplitude.

We expect the weights to amplify the high frequency content of the signal, and correct for incomplete wave field sampling and illumination angles. To better appreciate the challenges imposed by the geometry we consider the optimal

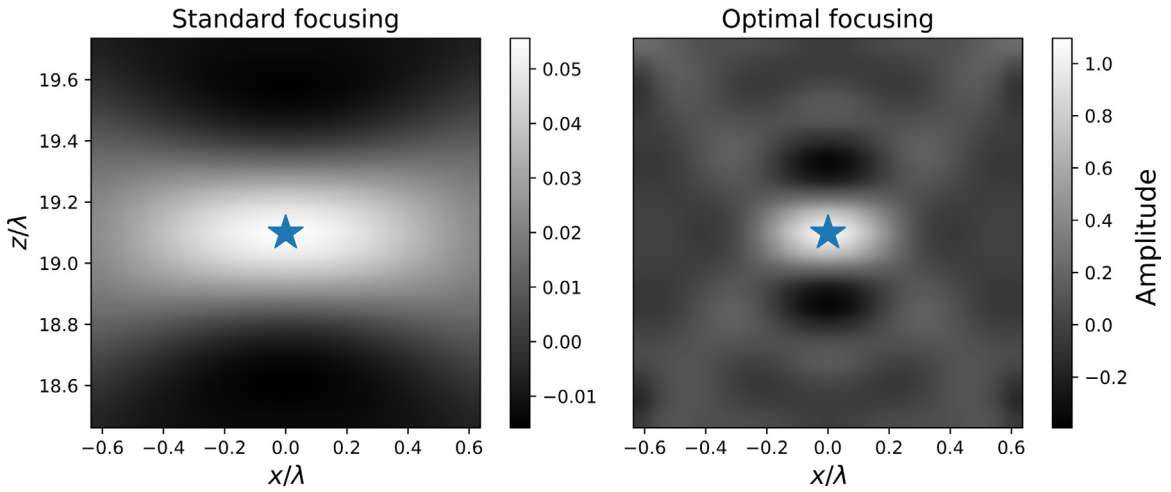

Fig. 2. Comparison of standard TR (left) and optimal TR images (right) for $\lambda \sim 80$ m at FOV. Notice the improvement of the focusing with the optimal weights.

and standard time-reversed wave fields with the cross-sections at the focusing level. The weights achieve improved localization of the source.

To estimate whether we achieve local or global focusing we calculate the weights for the FOV in Fig. 1 and analyze the standard and optimal time-reversed wave fields in a larger area. Fig. 4 shows the standard and optimal time-reversed wave fields for an area larger than FOV. The amplitude of the optimal time-reversed wave field inside FOV is masked by the amplitudes outside FOV. To better illustrate this behavior consider Fig. 5 where we show the cross-section at the source level of the optimal time-reversed wave field from Fig. 4. Notice that outside the FOV side lobes appear with amplitudes greater than the wave field inside the FOV, including the source location ($x = 0$), as pointed out above. This implies that we are only able to achieve local focusing in the vicinity of the source rather than everywhere in the medium. One could potentially increase the size of FOV to achieve a more global focusing at the expense of computational power (i.e., more data would be involved in the computation of the optimal weights assuming the grid spacing remains the same).

This finding regarding local focusing is not new. Francia [29] showed that it is possible to increase the resolution at the focal spot at the expense of large amplitudes at other locations in the imaging area. More recently, Rogers and Zheludev [34] showed that super-oscillatory lenses, which are developed to achieve optimal focusing, allow for imaging beyond the diffraction limit but produce adjacent side-bands as the field of view is increased, a consequence of super-oscillations. These oscillations arise when the wave field oscillates faster than its fastest Fourier component, and typically occur in regions where the wave field takes on small values [57].

To visualize super-oscillations we plot the natural logarithm of the absolute value of the time-reversed wave field as a function of space. Fig. 6 shows the magnitude plot in decibels (dB) of the cross-section in Fig. 5. Notice that regardless of how large we make our imaging area, the optimal wave field oscillates most rapidly in the vicinity of the source. Near the source location, where the optimization takes place, the optimal wave field oscillates faster than the smallest wavelength. These fast oscillations have a high frequency content that ultimately allows us to improve the resolution of the focal spot, indicating a connection between temporal and spatial resolution.

Now we consider the optimal and standard time-domain wave forms to visualize the optimal and standard signals. Fig. 7 shows the optimized time-reversed signal that is sent back from a receiver located at x = 1000 m. Notice the enrichment of high frequencies, which results in sharper focusing. However, this is not the only mechanism by which our algorithm improves the resolution of the focal spot. As we show in Section 5, the focusing is also improved when the algorithm is applied to monochromatic data, indicating that the resolution is improved at all frequencies. Periodic oscillations appear before and after the direct pulse at t = −1.8 s, with different temporal spacing at different receivers. Only oscillations within one dominant period around the direct arrival are necessary for focusing at the source location and focusing time $t = 0$. For earlier and later times the reverberations do not contribute to focusing at $t = 0$ and are a result of imposing spatio-temporal focusing instead of only spatial focusing. To validate this reasoning we consider the temporal compression of the optimal time-reversed wave field at the source location for different sizes of the time-window used of the signals that are sent into the medium. The left panel of Fig. 8 shows the amplitude of the time-reversed wave field at the source location as a function of time for different window sizes around the direct arrival at t = −1.8 s, where the dominant period is 0.075 s. Notice that as we decrease the size of the window around the direct arrival the temporal delta function is distorted (there are now nonzero amplitudes at $t \neq 0$). This observation implies that we need these reverberations to achieve temporal focusing. The right panel of Fig. 8 shows cross sections at the source level for the wave field focused with the signals radiated from the different window sizes. Notice that as we decrease the window size the

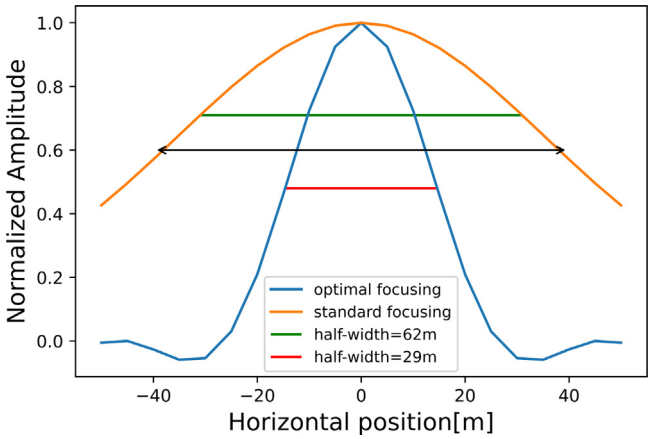

Fig. 3. Cross section at source level for standard and optimal focusing. Optimal half-width (red line) is below half the dominant wavelength ∼40 m. Standard half-width (green line) is about 3/4 of the dominant wavelength. The two headed black arrow indicates one full dominant wave length.

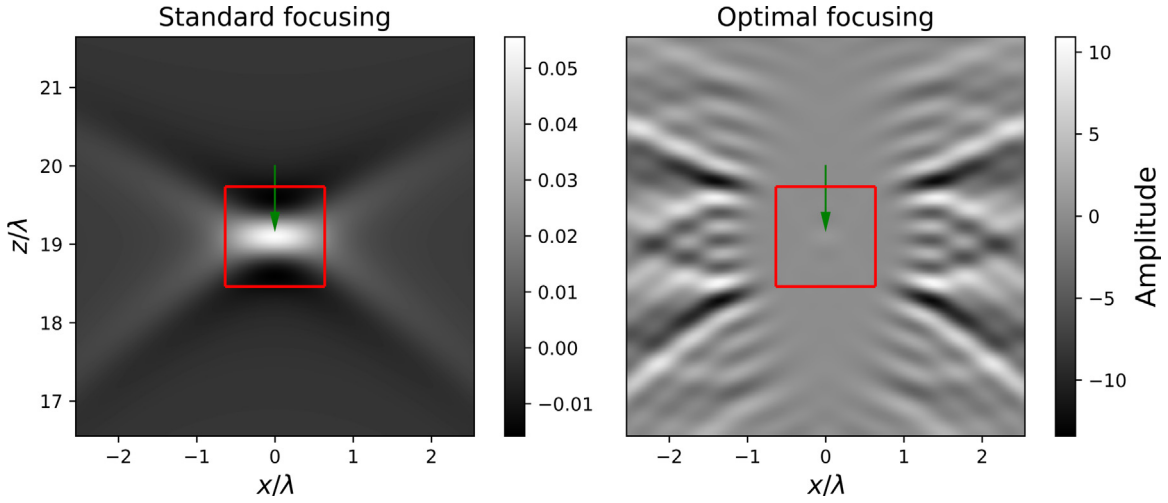

Fig. 4. Comparison of standard TR (left) and optimal TR images (right) for $\lambda \sim 80$ m for a region larger than FOV. The red box indicates the FOV which corresponds to the same dimensions as Fig. 2. The green arrow indicates the location of the focal spot.

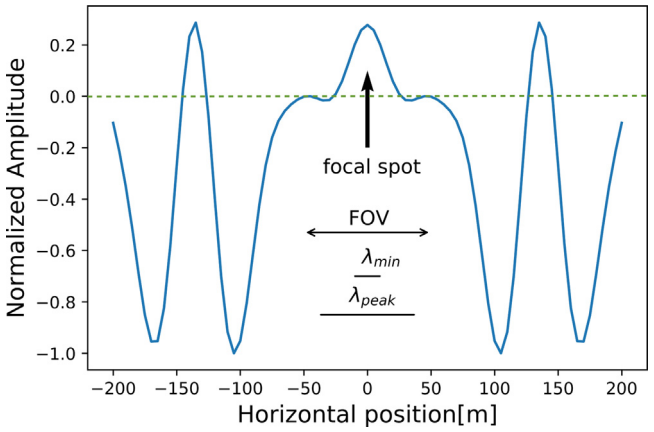

Fig. 5. Cross section at source level of optimal focusing using an imaging area with horizontal size of 400 m around the source location (−200 to 200 m).

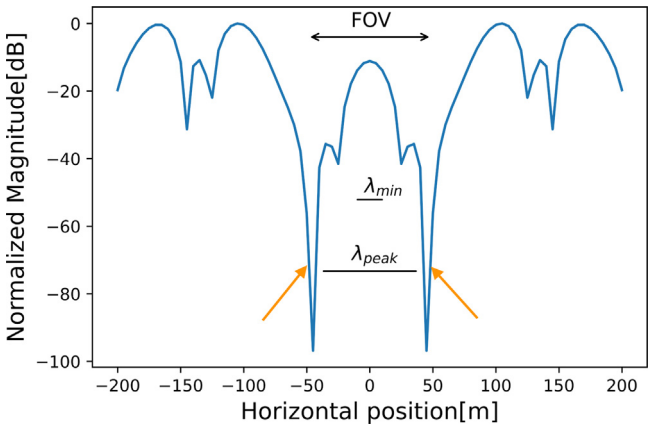

Fig. 6. Magnitude plot of the cross-section in Fig. 5. The orange arrows indicate areas of super-oscillations.

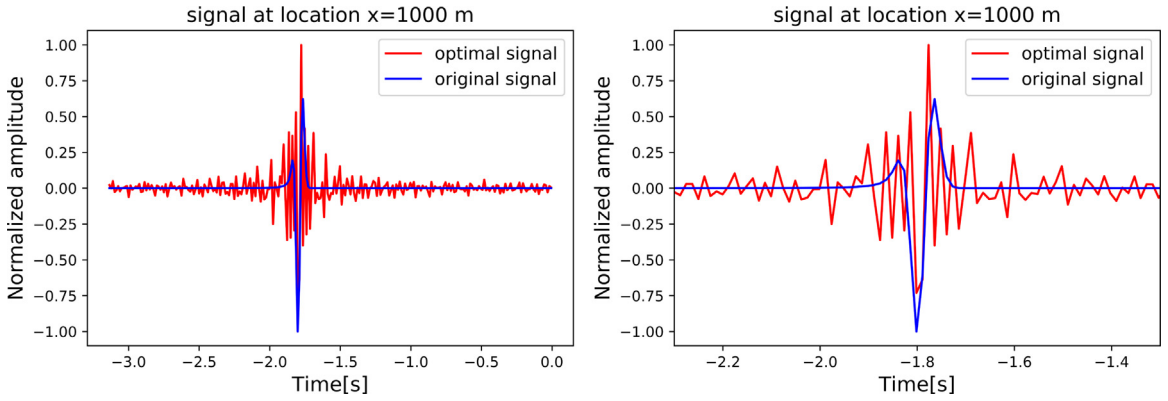

Fig. 7. Comparison of original (i.e., $G(\mathbf{x}_i, -t_0, \mathbf{x}_0, -t) * S(-t)$) and optimal (i.e., $\sigma_i(\mathbf{x}_i, t) * G(\mathbf{x}_i, -t_0, \mathbf{x}_0, -t) * S(-t)$) signals for receiver at x=1000 m with normal view (left) and zoom-in view (right). The focusing time at the source location corresponds to $t = 0$.

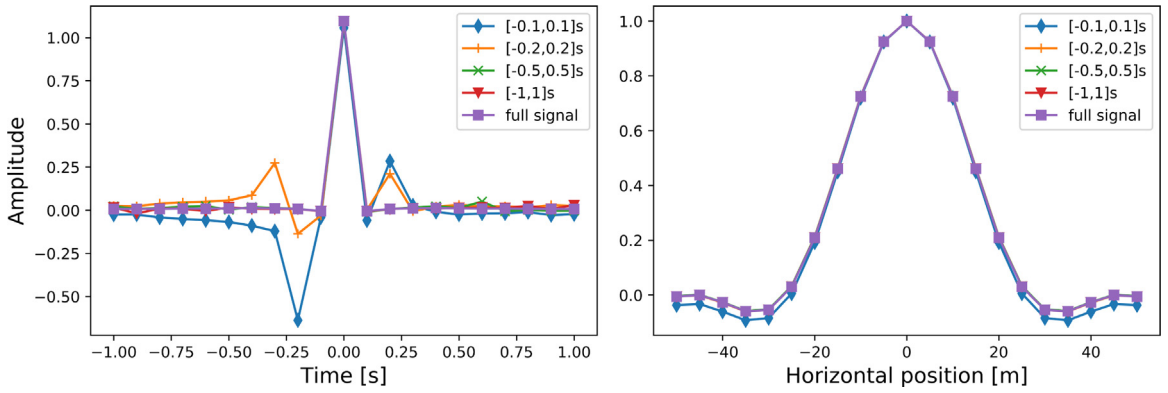

Fig. 8. Amplitude at source location as a function of time for different window sizes around the direct arrival in Fig. 7 (left). Cross-section at source level for different window sizes around the direct arrival in Fig. 7 (right).

spatial focusing at time $t = 0$ remains mostly unaffected (i.e., no significant change in the focal spot). The reverberations outside the windows do not affect the amplitude of time-reversed wave field at the source location at $t = 0$ but distort the amplitude of the wave field at other times for the same location. This means that these reverberations are necessary to maintain the temporal focusing but do not affect spatial focusing.

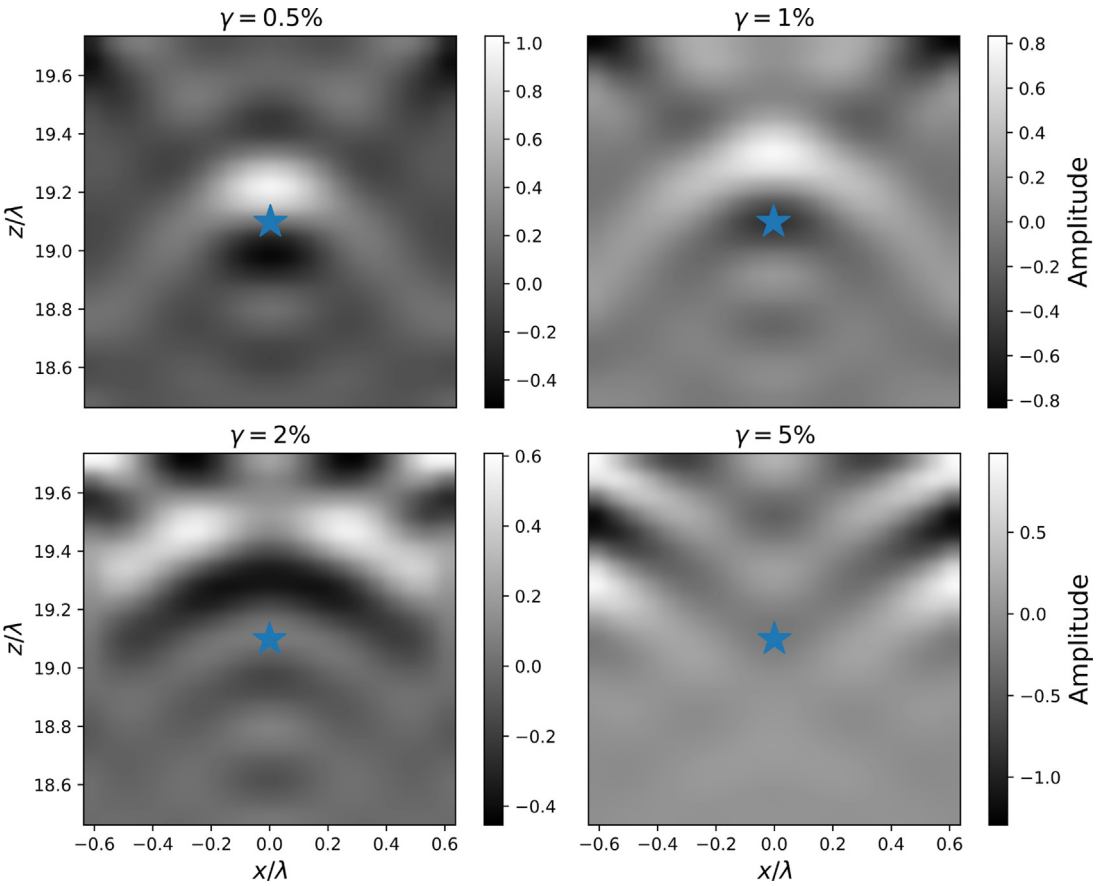

Fig. 9. Optimal time-reversed images for different levels of velocity perturbation. The blue star indicates the true source location.

4. Sensitivity analyses

To investigate the robustness of the optimal focusing we consider variations in the background velocity and source location, as well as the effect of adding band-limited noise to the recorded signal before time-reversal.

4.1. Velocity perturbation

First, we calculate the weights for the true velocity of the medium. We then perform the back-propagation using a perturbed velocity. Denoting γ as the percentage variation of the true velocity, we consider $\gamma = 0.5$, 1.0, 2.0, and 5.0%. Fig. 9 shows that the quality of focusing degrades with increasing velocity perturbation. An erroneous velocity gives the wrong source location and increases the width of the focal spot. This means that if one wants to achieve accurate focusing (both in terms of location and size of the focal spot), one needs to know the velocity of the medium with great accuracy. For our experimental set-up we need to know the velocity of the medium within a 1% error such that the focal spot is shifted but not degraded. This sensitivity to velocity errors is similar in the unweighted time-reversed wave field.

4.2. Source location

Now suppose that the tested and reference source locations are different. To study this scenario we first calculate the weights corresponding to a fixed source location (center of the FOV). Using those weights we perform the time-reversal process for waves which originate from other locations within the field of view. Fig. 10 shows that the optimal weights allow for focusing of events at locations different than the reference location for which the weights were calculated. Artifacts on the boundary of FOV arise when the distance between the new and original source location increases. Notice that the imaging is more sensitive to horizontal than vertical changes of the source location. This is due to the fact that a horizontal shift induces a relative phase shift among receivers, whereas a vertical shift in source location induces a constant phase shift across all receivers because of the symmetry of the experiment.

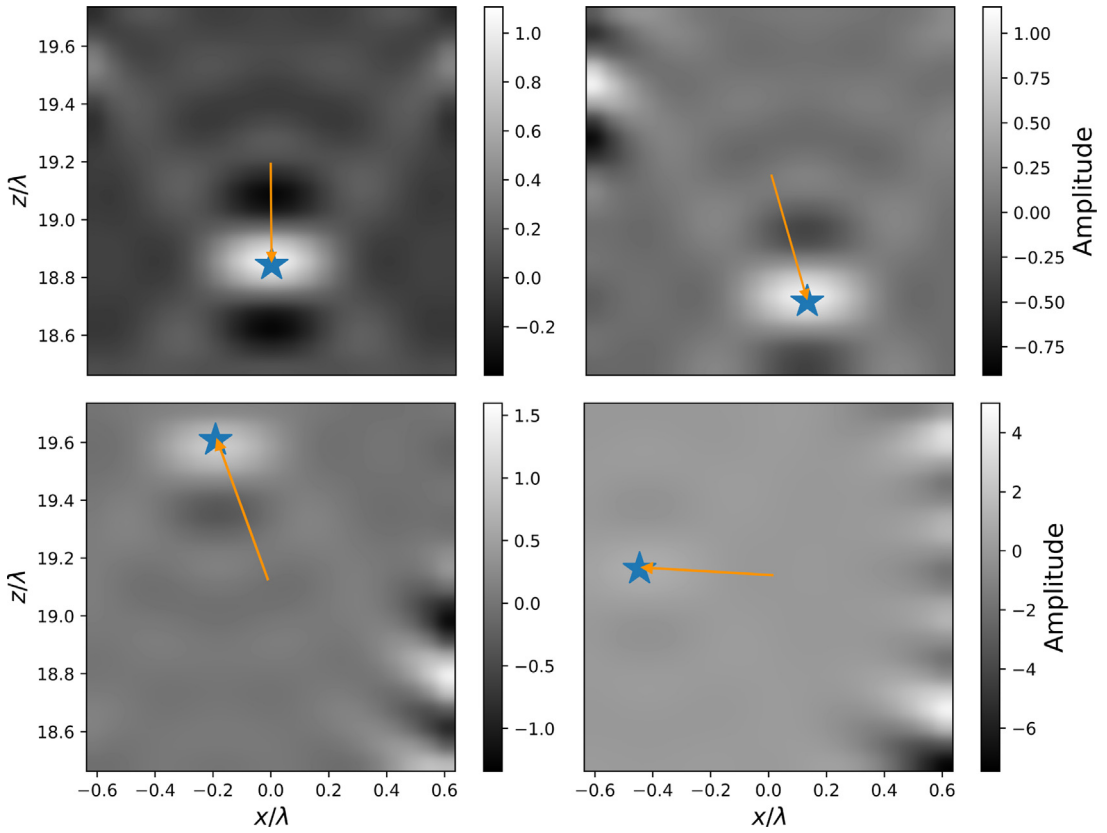

Fig. 10. Optimal time-reversed images for different source locations using the weights corresponding to the reference source location (x_0, z_0)=(0,1500). The orange arrow provides a measure of the distance between the reference location used to compute the weights and the tested source location.

4.3. Noisy inversion

Let us consider the effect of noisy recorded data. To this end we add band-limited (0.32 to 40 Hz) uncorrelated random noise to the recorded signal, defined as $\frac{\text{mean}(|\text{noise}|)}{\text{mean}(|\text{signal}|)} \times 100 = \text{noise }\%$. We then perform optimal imaging using the weights calculated for data without noise. One would expect the weights to amplify the noise, and consequently the optimal TR image to be degraded. Figs. 11 and 12 show that noise degrades the quality of focusing. We can introduce up to 5% noise without distorting the focal spot significantly. Our algorithm is sensitive to noise, especially if the noise has high frequency content. This occurs because we are amplifying higher frequencies. To make optimal imaging more robust to noise one could filter out the highest frequencies at the expense of resolution improvement.

5. Resolution analyses

We make use of the full-width half-maximum (FWHM) to measure the resolution improvement. For simplicity we make the resolution comparisons in terms of amplitudes rather than intensities. As we discussed in Section 3 (Fig. 3), the standard focusing gives a FWHM of 62 m whereas the optimal focusing gives a FWHM of 29 m, a resolution improvement of more than a factor of 2. To avoid ambiguity in dealing with the resolution of a polychromatic wave field we show the cross-section at the source level of the TR wave field for several frequencies in Fig. 13. This way of analyzing resolution allows us to understand how well our algorithm improves the resolution at the focal spot (i.e., considering a monochromatic rather than a polychromatic wave field), and confirms that rather than just boosting the high frequency content of the signal, we improve the resolution at all frequencies by the used weighting. Fig. 13 shows the resolution improvement at different individual frequencies. Even for each single frequency the focusing is improved. Notice that the improvement is most pronounced at low frequencies, where the resolution is poor. At higher frequencies there is still an improvement in the compression of the focal spot but not as significant as for lower frequencies. The way our algorithm is constructed (i.e., frequency by frequency) allows us to improve the resolution at every single frequency, with the amount of improvement varying across the frequency spectrum.

Alternatively, there are two other ways in which we can empirically study resolution improvement. The first approach consists of using a horizontal dipole source in generating the source–receiver data rather than an impulse monopole

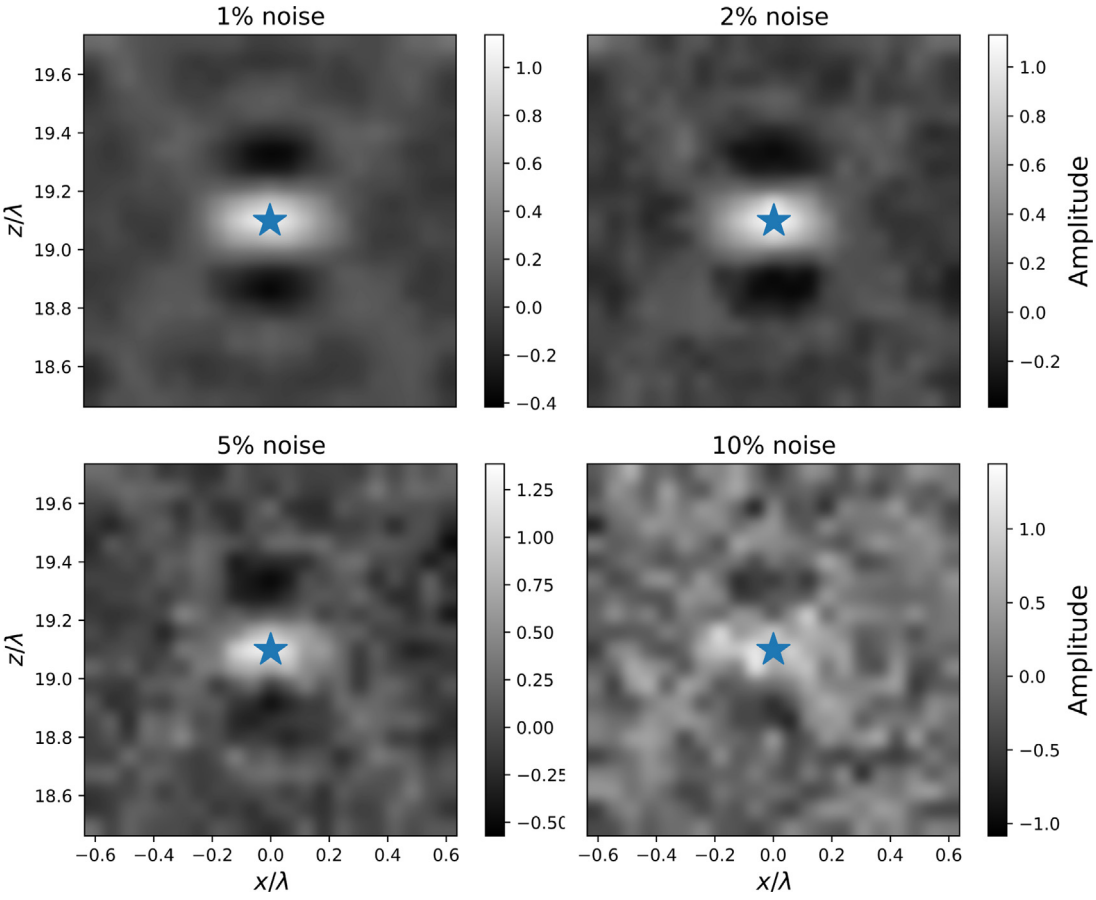

Fig. 11. Optimal time-reversed wavefield for different noise.

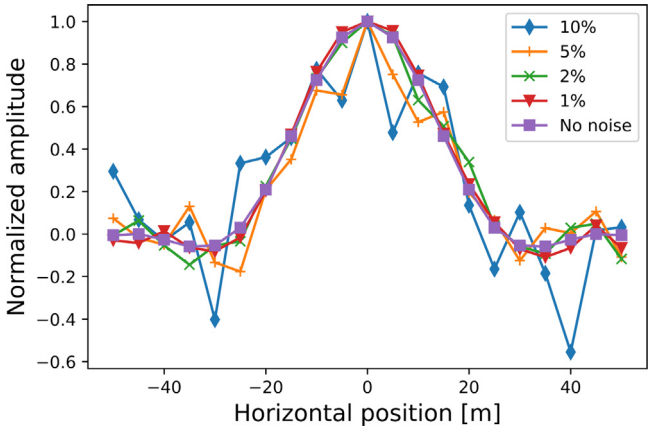

Fig. 12. Cross sections of optimal time-reversed wave fields from Fig. 11.

source, and perform the time-reversal operation using the optimal weights calculated for the spatio-temporal delta function. Assuming infinite resolution, we should obtain a mathematical dipole (i.e., infinitesimally small) after performing the TR operation. However, since resolution is limited, we can use the horizontal separation between the positive and negative ends of the dipole to measure resolution. Fig. 14 shows the standard and optimal TR wave fields for a horizontal dipole source, and their corresponding horizontal cross-sections at the source level. Standard imaging shows a separation of 70 m between minimum and maximum, whereas optimal imaging shows a separation of just 30 m. This corresponds to improving the resolution by a factor of 2.3. Notice also that the optimal time-reversed wave field shows improvement

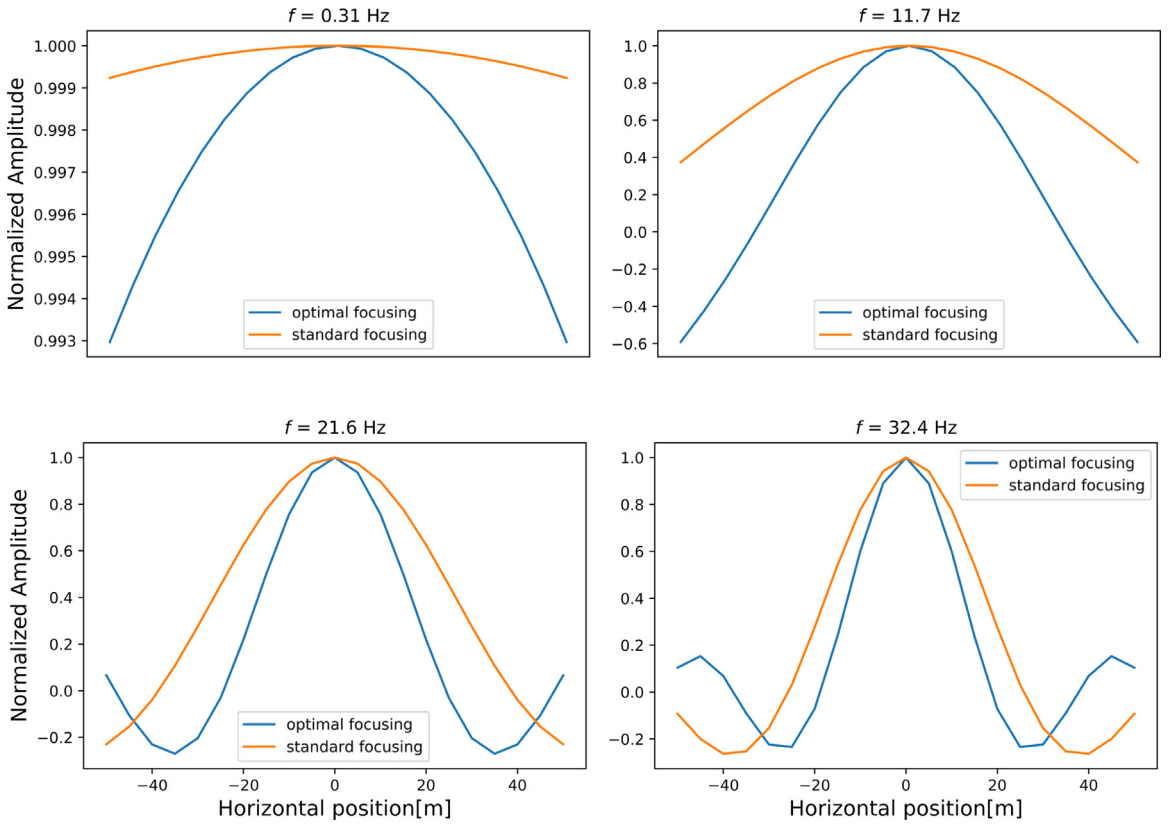

Fig. 13. Cross-sections of time-reversed wave fields for standard and optimal wave fields at the source level at focusing time for different frequencies.

of the vertical resolution. The second approach consists of increasing the upper end of the frequency bandwidth as well as the peak frequency of the source wavelet until the cross-section of the standard TR wave field at the source level matches most closely that of the optimal wave field computed with the initial frequency bandwidth. Fig. 15 shows that for the optimal and standard waveforms to match we need to increment the maximum and the peak frequency in the standard TR experiment. Notice that for the focal spots to match we need to go beyond the original maximum frequency of 40 Hz.

6. Variation of optimal weights

6.1. Frequency variation of the optimal weights

We begin by considering how the magnitude of the weights change with frequency for several spatial locations. This is useful to understand the effect of the weights in the improved resolution of the time-reversed wave field as a function of frequency. For illustrative purposes we only consider receivers located at $x = 200, 500, 800, 1000$ m. Fig. 16 shows the natural logarithm of the frequency spectrum of the weights at four different locations. Despite their seemingly complicated nature the high frequencies are amplified but the signal at lower frequencies is modulated, as previous explained in Section 5. At all frequencies the resolution is improved which ultimately allows us to significantly reduce the size of the focal spot of the time-reversed wave field.

6.2. Spatial variation of the optimal weights

To appreciate the contribution of the different receivers to the improved resolution of the time-reversed wave field we show in Fig. 17 the spatial variation of the real part of the weights across the receiver array for different frequencies. We omit the imaginary part since it has amplitudes much smaller than its real counterpart ($\simeq$5%). First, notice that the weights are symmetric around the source position ($x = 0$). This is expected from the symmetric array geometry. The weights are oscillatory in space with a fairly constant wavelength across the array with a weak amplitude modulation, except near the end points of the array. Furthermore, the weights oscillate faster in space as the temporal frequency f increases. Fig. 17 also shows that the highest amplitude across the array increases with frequency. This means that the

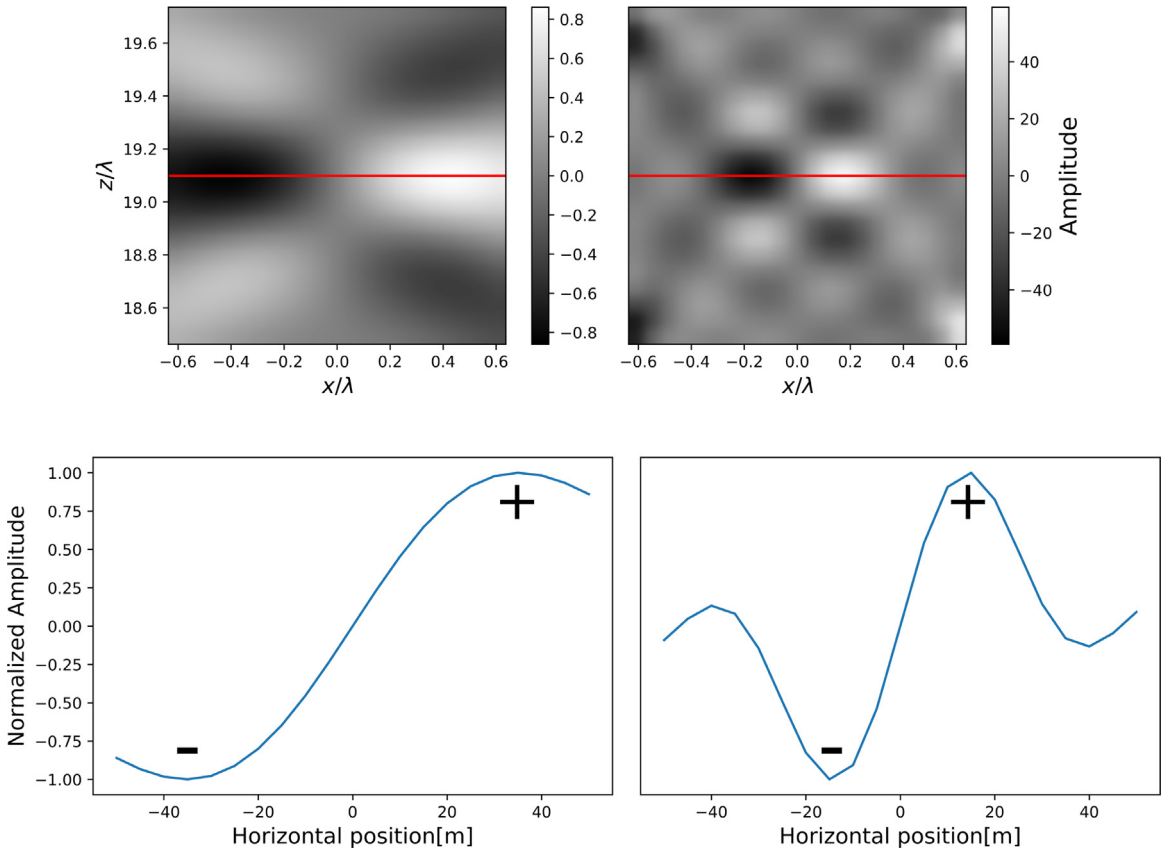

Fig. 14. Time-reversed standard (upper left) and optimal (upper right) wave fields for a horizontal dipole source, and their corresponding standard (lower left) and optimal (lower right) horizontal cross-sections at the source level. The black horizontal line marks the source level and the location of the cross sections in the lower panels. The negative and positive signs indicate minimum and maximum, respectively.

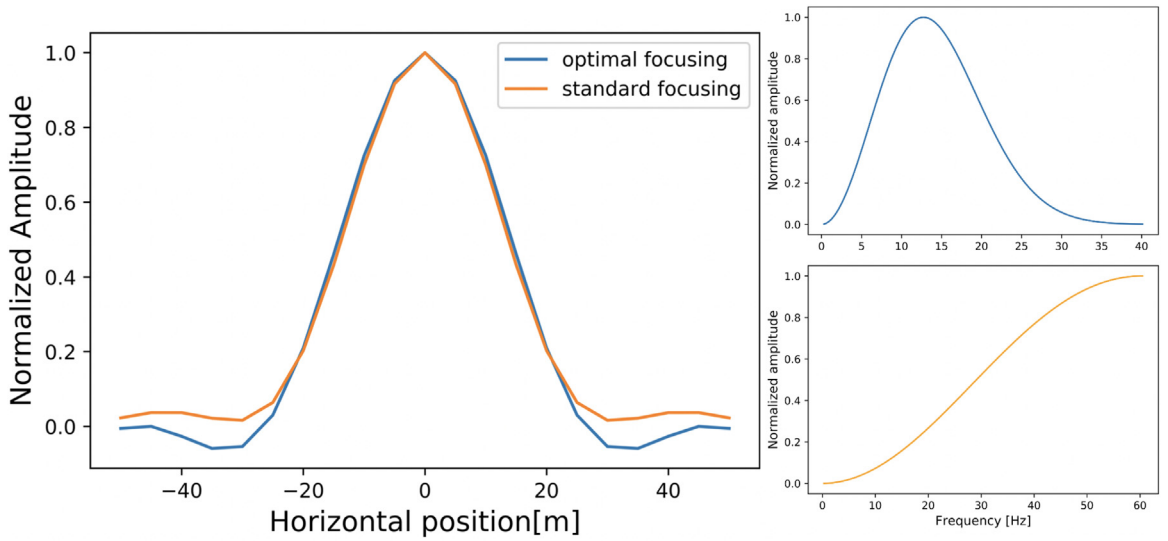

Fig. 15. Cross section at source level for standard and optimal focusing. The standard focusing waveform is computed using the source wavelet in the lower right panel ($f_{peak} = f_{max} = 60.47$ Hz). The optimal waveform is computed using the source wavelet in the upper right panel ($f_{peak} = 12.73$ Hz, $f_{max} = 40$ Hz).

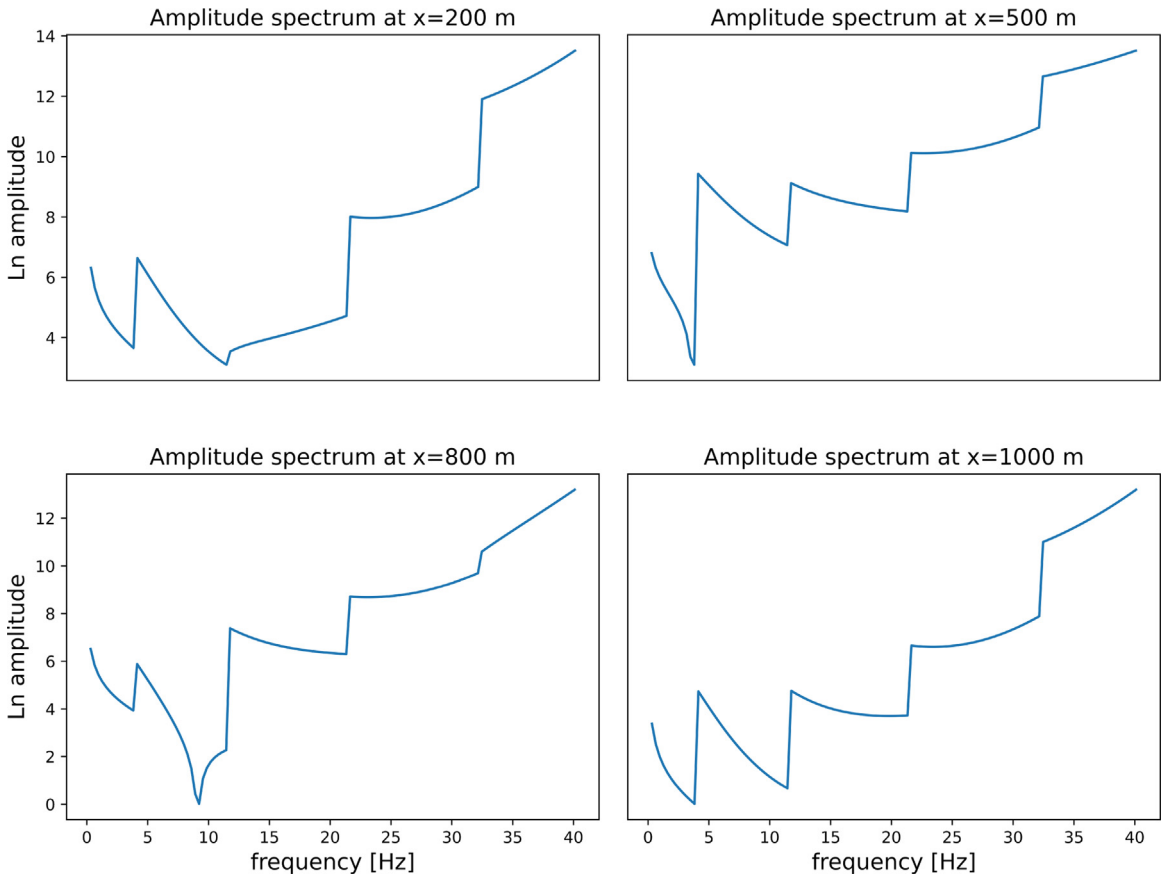

Fig. 16. Natural logarithm of the frequency spectrum of the weights at four different locations.

algorithm boosts the higher frequencies, which together with the modulation of all other frequencies results in resolution improvement of the focal spot for broadband waveforms.

As mentioned previously, the imaginary part of the weights is much smaller than the real part at all frequencies. This implies that rather than applying sophisticated phase changes, it is only necessary to multiply each receiver data by real weights with a variable sign. Francia [29] showed that it is possible to improve the resolution of a focal spot by superimposing different ring apertures. To superimpose the different ring apertures he assigns real coefficients, which signify aperture transparency, to each of the rings. The similarity between his and our results suggests that, as mentioned before, multiplying the receiver data by real weights with a variable sign suffices to achieve improved resolution. In addition, the weights shown in Fig. 17 resemble the Tchebyscheff polynomials widely used in beam forming [58]. As mentioned above, the weights retrieved by our algorithm are almost real, which is in agreement with the work of Dolph [58]. The fact that our algorithm produces these weights in the case of a homogeneous medium and a uniform line array establishes a connection with the optimal weights derived by Dolph [58] for a regular array in a homogeneous medium. Our algorithm, which converges to the Tchebyscheff polynomials in our set-up, can also be applied to irregular arrays, as opposed to using the Tchebyscheff polynomials for beam forming. Gallaudet and de Moustier [59] show an example of the modifications that one must perform when doing beam forming via Tchebyscheff polynomials with irregular arrays.

7. Focusing in scattering media

To test the robustness and flexibility of our algorithm we now consider an inhomogeneous medium which contains scatterers and an irregular receiver line. We remind the reader that rather than comparing the size of the focal spot to the results obtained in Section 3, the aim of this section is to demonstrate that our algorithm improves the resolution of the focal spot even when the medium is complicated and the receiver line is irregular. We illustrate the geometrical set-up in Fig. 18. We place 50 isotropic scatterers randomly between 400 and 1400 m in the vertical direction and -200 to 200 m in the horizontal direction. The location of the source and the coordinates of FOV as well as the grid spacing are the same as in the experiments in Section 3. We place 30 receivers at random locations along a horizontal line at $z = 0$ between -300 and 300 m, which allows us to investigate focusing with irregular line arrays. We compute the wave field

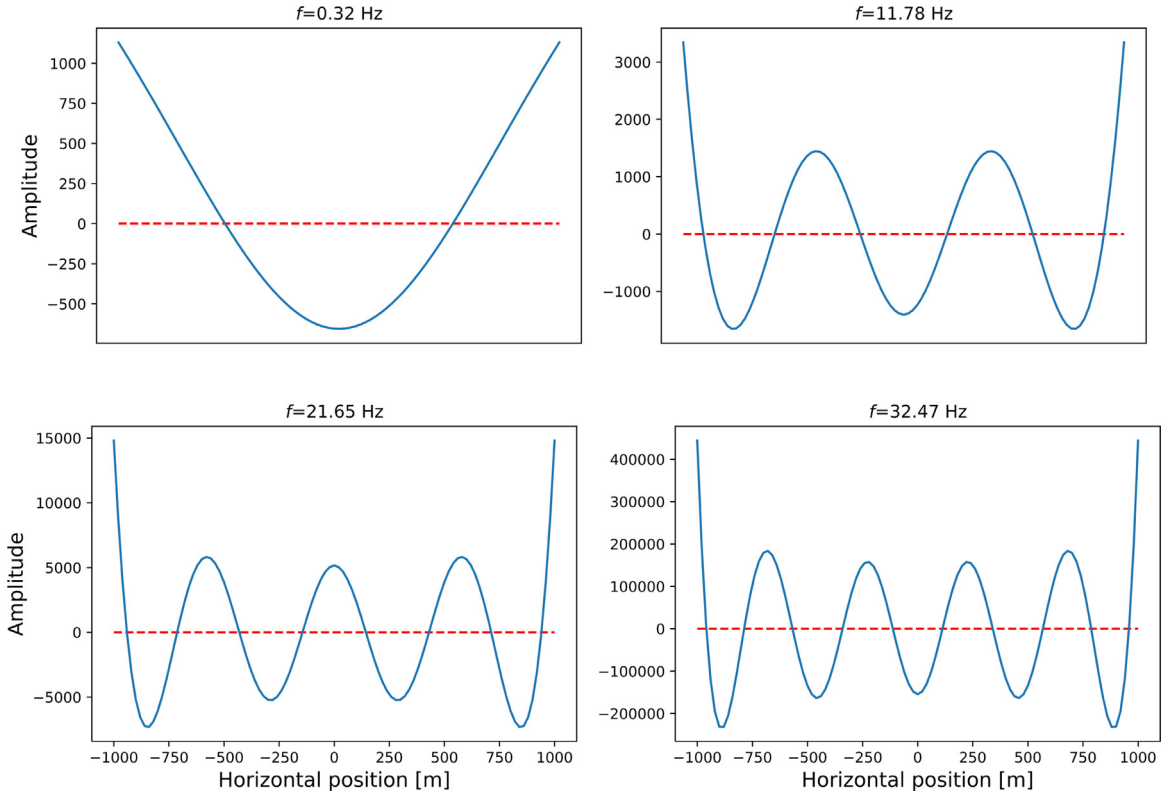

Fig. 17. Spatial variation of the real part of weights across the receiver array for different frequencies.

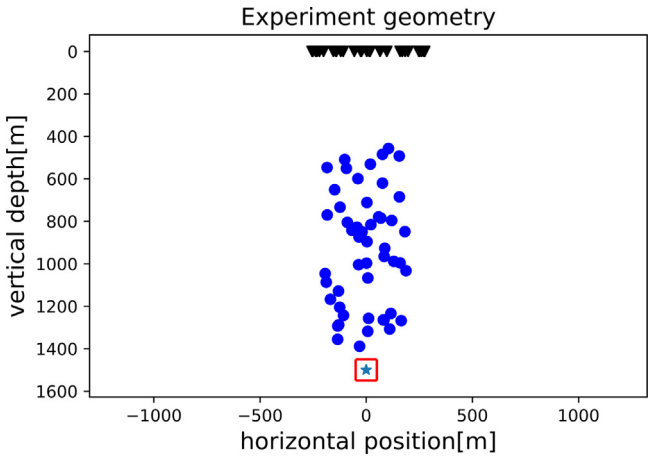

Fig. 18. Illustration of the geometrical set-up for focusing with embedded scatterers and an irregular receiver array. The blue star indicates the location of the source, the red box the field of view, the blue dots the locations of the point scatterers, and the black triangles the receiver array elements.

that propagates from the source to the receivers using the multiple isotropic point scattering (MIPS) solution [60]. This approximation is based on Foldy's method [61], and consists of describing the total wave field in the frequency domain as a sum of the direct wave and the scattered wave field from a set of scatterers

$$\Psi(\mathbf{r}) = \Psi_0(\mathbf{r}) + \sum_{i=1}^{n} G^{(0)}(\mathbf{r}, \mathbf{r}_i) A_i \Psi(\mathbf{r}_i), \tag{10}$$

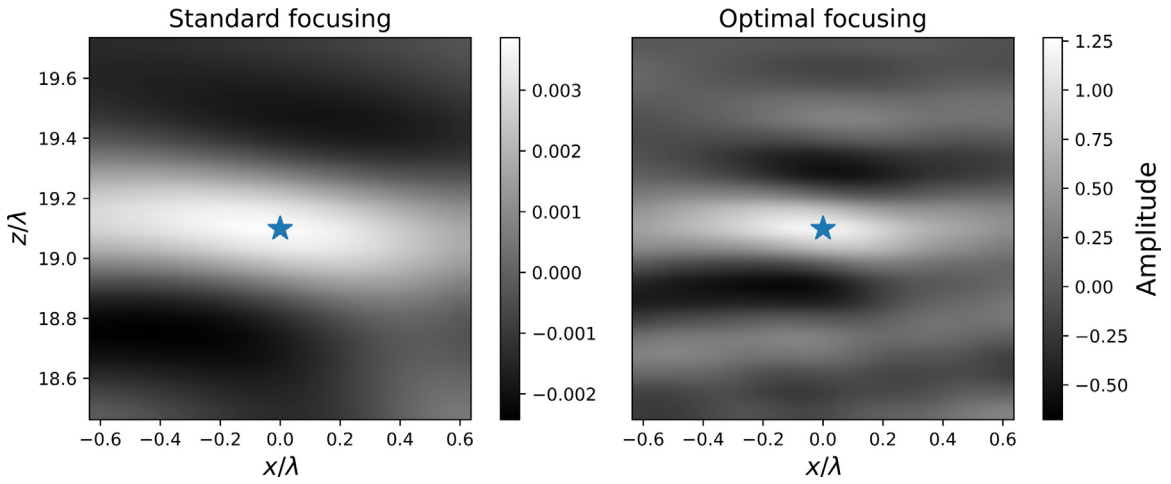

Fig. 19. Comparison of standard TR (left) and optimal TR images (right) for $\lambda \sim 80$m at FOV in the presence of scatterers. The blue star indicates the source location.

where n is the number of scatterers, A_i is the i^{th} scattering amplitude which is a complex number in the frequency domain, and $G^{(0)}(\mathbf{r}, \mathbf{r}_i)$ is the 2-D Green's function used in Section 3. For details regarding the numerical computations of the total wave field under the MIPS approximation see the appendix in Groenenboom and Snieder [60]. We choose $|A_i| = 3.0$ for all scatterers, and compute the imaginary and real components of the scattering amplitude as $\Im(A_i) = -|A_i|^2/4$ and $\Re(A_i) = \sqrt{-\Im(A_i)(4 + \Im(A_i))}$, respectively. The velocity of the background medium, the frequency parameters and the source signal are the same as in Section 3.

The procedure for computing the standard and optimal time-reversed wave fields is the same as before, which facilitates the optimization.

Fig. 19 shows both standard (left-panel) and optimal (right-panel) focusing in the presence of embedded scatterers. As for the examples in Section 3 for a homogeneous medium and a regularly spaced receiver array, our algorithm improves the resolution of the focal spot. We attain resolution enhancement both along the vertical and horizontal directions. Our algorithm thus performs well in both homogeneous and inhomogeneous media, and we are able to reduce the size of the focal spot in both cases. In addition, our algorithm is able to handle irregular arrays without any modifications. Contrary to focusing in a homogeneous medium with a uniform line array, the optimal weights do not resemble Tchebyscheff polynomials, instead they have a complicated oscillatory structure which we refrain from showing here.

8. Discussion

The focusing method we propose allows us to improve the resolution of focusing in a time-reversal numerical simulation, and may be extended to other focusing functions and source distributions. The extent to which the resolution is improved will ultimately depend on the Green function which describes the propagation of the wave field to be time reversed and the type of model that we use (strongly vs weakly scattering media). The optimization of the focal spot is confined to the field of view, as shown in Section 3, Fig. 4. Outside of the field of view the amplitude of the optimal time-reversed wave field is significantly larger than inside the FOV and masks the focal spot. This is related to the concept of super-gain antennas with which it is possible to increase the resolution of the focal spot in a given FOV at the expense of larger amplitudes outside FOV [29]. Section 4 addresses the applicability of our method. Firstly, we point out that we are able to handle weak velocity errors, as illustrated in Fig. 9. We are also able to obtain good focusing in test locations within FOV different to the reference source location (Fig. 10). For the used geometry our method is able to handle band-limited noise up to 5% (Fig. 11). One could filter out the highest frequencies at the expense of resolution improvement to make the optimal imaging more robust to noise. Our resolution analyses show that we do not only boost high frequencies but also improve the resolution at all frequencies (Fig. 13). We are also able to obtain a significant resolution improvement for a horizontal dipole source which is very promising for applications that involve complex sources (Fig. 14). We find that for standard TR to closely match optimal TR we have to increase the upper end of the frequency bandwidth as well as the peak frequency of the source wavelet by a significant amount (Fig. 15). The frequency spectra of the optimal weights change in a complicated manner but illustrate that we do not just boost high frequencies; we improve the focusing at each individual frequency (Fig. 16). Lastly, we show that the weights oscillate faster in space as the temporal frequency increases, providing a link between spatial and temporal frequency improvement. For a homogeneous medium and a uniform line array we find that for a given frequency the weights have a fairly constant wavelength across the array with weak amplitude modulation (Fig. 17). In this set-up the optimal weights resemble the Tchebyscheff polynomials used in earlier beam forming. Our algorithm does not require any extra modifications when dealing with irregular arrays or inhomogeneous media, as shown in Section 7.

9. Conclusions

We have shown that it is possible to locally improve the resolution of the TR wave field in both homogeneous and heterogeneous media, even at very large distances from the source (19 dominant wavelengths) by applying a complex filter to the signal before time-reversal. In practice this is similar to techniques such as beam forming, spatial light modulation or antenna focusing [62], where some type of spatial filtering is applied. Our technique is directly applicable to polychromatic wave fields as opposed to the techniques mentioned above and the focusing is achieved in space and time. In this paper we optimize the signal to be time-reversed rather than asking for an arbitrarily optimal signal that allows focusing after propagation of the wave field through an imaging system. To calculate the optimal weights we use a modified Backus–Gilbert approach which guarantees the focal spot to be localized at the source. Neither evanescent waves nor resonant multiples are needed to achieve enhanced focusing if we know how the original signal must be modulated. We find artifacts remain in the optimal TR images. The weights partially compensate for the limited geometry and the incomplete wave field sampling by modifying the frequency spectrum of the signal that is time-reversed. Optimal imaging is robust to errors in the source location. This is important because we do not always know the exact source location. The fact that we obtain proper focusing in locations different from the reference source implies that if we have full information of a control point in the field of view we can achieve focusing in other points within the FOV. To achieve proper focusing we also need to know the velocity of the medium accurately, this drawback arises from the nature of time-reversal. Additive noise degrades the quality of focusing, in particular when the noise has high frequency content. In addition, we find that even with optimization techniques, only local focusing is possible. Regardless of the metric used to study resolution enhancement the optimal weights improve the localization of the focal spot by several factors. We showed that the algorithm does not only boost the highest frequencies but that it also increases the resolution of the focal spot for monochromatic waves. The optimal weights oscillate faster across the receiver array as the temporal frequency increases. In addition, the amplitude of the weights increase with frequency, resulting in higher resolution. In the case of a homogeneous medium and a uniform line array our algorithm retrieves weights that resemble the Tchebyscheff polynomials widely used in beam forming. Our proposed method also shows focusing improvement in inhomogeneous media, and no extra modifications are needed when dealing with irregular arrays.

CRediT authorship contribution statement

Manuel A. Jaimes: Conceptualization, Methodology, Preparation of manuscript, Analysis of results, Interpretation, Investigation, Data curation. **Roel Snieder:** Supervision, Funding acquisition, Project administration, Editing and reviewing manuscript.

Declaration of competing interest

The authors declare that they have no known competing financial interests or personal relationships that could have appeared to influence the work reported in this paper.

Acknowledgments

This work was supported by the Consortium Project on Seismic Inverse Methods for Complex Structures at the Center for Wave Phenomena, Colorado School of Mines. We thank Dr. Kees Wapenaar from Delft University of Technology for fruitful discussions about resolution analyses. We also thank Dr. Paul Martin from Colorado School of Mines for a thorough manuscript revision. In addition, we thank 2 anonymous reviewers for their constructive criticism which aided in improving the manuscript.

References

[1] F. Broggini, R. Snieder, K. Wapenaar, Focusing the wavefield inside an unknown 1D medium: Beyond seismic interferometry, Geophysics 77 (5) (2012) A25–A28.
[2] D.R. Jackson, D.R. Dowling, Phase conjugation in underwater acoustics, J. Acoust. Soc. Am. 89 (1) (1991) 171–181.
[3] M. Tanter, J.-L. Thomas, M. Fink, Time reversal and the inverse filter, J. Acoust. Soc. Am. 108 (1) (2000) 223–234.
[4] M. Tanter, J.-F. Aubry, J. Gerber, J.-L. Thomas, M. Fink, Optimal focusing by spatio-temporal inverse filter. I. Basic principles, J. Acoust. Soc. Am. 110 (1) (2001) 37–47.
[5] A. Parvulescu, C. Clay, Reproducibility of signal transmissions in the ocean, Radio Electron. Eng. 29 (4) (1965) 223.
[6] M. Fink, Time reversed acoustics, Phys. Today 50 (3) (1997) 34–40.
[7] J. Billingsley, R. Kinns, The acoustic telescope, J. Sound Vib. 48 (4) (1976) 485–510.
[8] J. Capon, High-resolution frequency–wavenumber spectrum analysis, Proc. IEEE 57 (8) (1969) 1408–1418.
[9] Y. Jin, Y. Jiang, J.M. Moura, Time reversal beamforming for microwave breast cancer detection, in: 2007 IEEE International Conference on Image Processing, IEEE, San Antonio, TX, USA, 2007, pp. V – 13–V – 16.
[10] C.A. Viteri-Mera, F.L. Teixeira, Equalized time reversal beamforming for frequency-selective Indoor MISO channels, IEEE Access 5 (2017) 3944–3957.
[11] Q. Xu, C. Jiang, Y. Han, B. Wang, K.J.R. Liu, Waveforming: An overview with beamforming, IEEE Commun. Surv. Tutor. 20 (1) (2018) 132–149.

[12] S.-W. Chung, Y.-K. Kim, Design and fabrication of 10x10 micro-spatial light modulator array for phase and amplitude modulation, Sensors Actuators A 78 (1) (1999) 63–70.
[13] I. Lokmer, G.S. O'Brien, D. Stich, C.J. Bean, Time reversal imaging of synthetic volcanic tremor sources, Geophys. Res. Lett. 36 (12) (2009) L12308.
[14] C.S. Larmat, R.A. Guyer, P.A. Johnson, Time-reversal methods in geophysics, Phys. Today 63 (8) (2010) 31–35.
[15] R. Lu, M.N. Toksö, M.E. Willis, Locating microseismic events with time reversed acoustics: A synthetic case study, 2008.
[16] S.A. Shapiro, Microseismicity: A Tool for Reservoir Characterization, Number 2, Education tour series CIS, Eage, Houten, 2008.
[17] G.T. Schuster, Reverse-time migration = generalized diffraction stack migration, in: SEG Technical Program Expanded Abstracts 2002, Society of Exploration Geophysicists, 2002, pp. 1280–1283.
[18] G. Edelmann, H. Song, S. Kim, W. Hodgkiss, W. Kuperman, T. Akal, Underwater acoustic communications using time reversal, IEEE J. Ocean. Eng. 30 (4) (2005) 852–864.
[19] B.E. Anderson, T.J. Ulrich, P.-Y.L. Bas, J.A. Te. Cate, Three-dimensional time reversal communications in elastic media, J. Acoust. Soc. Am. 139 (2) (2016) EL25–EL30.
[20] G. Micolau, M. Saillard, P. Borderies, DORT Method as applied to ultrawideband signals for detection of buried objects, IEEE Trans. Geosci. Remote Sens. 41 (8) (2003) 1813–1820.
[21] G. Lerosey, J. de Rosny, A. Tourin, A. Derode, G. Montaldo, M. Fink, Time reversal of electromagnetic waves, Phys. Rev. Lett. 92 (19) (2004) 193904.
[22] N. Chakroun, M. Fink, F. Wu, Time reversal processing in ultrasonic nondestructive testing, IEEE Trans. Ultrason. Ferroelectr. Freq. Control 42 (6) (1995) 1087–1098.
[23] M. Fink, G. Montaldo, M. Tanter, Time-reversal acoustics in biomedical engineering, Annu. Rev. Biomed. Eng. 5 (1) (2003) 465–497.
[24] M. Fink, W.A. Kuperman, J.-P. Montagner, A. Tourin (Eds.), Imaging of complex media with acoustic and seismic waves, in: Volume 84 of Topics in Applied Physics, Springer, Berlin, 2002.
[25] R. Snieder, A Guided Tour of Mathematical Methods: for the Physical Sciences, second ed., Cambridge University Press, 2004.
[26] D. Cassereau, M. Fink, Time-reversal of ultrasonic fields. III. Theory of the closed time-reversal cavity, IEEE Trans. Ultrason. Ferroelectr. Freq. Control 39 (5) (1992) 579–592.
[27] P. Blomgren, G. Papanicolaou, H. Zhao, Super-resolution in time-reversal acoustics, J. Acoust. Soc. Am. 111 (1) (2002) 230–248.
[28] A. Maznev, O. Wright, Upholding the diffraction limit in the focusing of light and sound, Wave Motion 68 (2017) 182–189.
[29] G. Francia, Super-gain antennas and optical resolving power, Il Nuovo Cimento 9 (3) (1952) 426–438.
[30] J.-L. Thomas, M. Fink, Ultrasonic beam focusing through tissue inhomogeneities with a time reversal mirror: application to transskull therapy, IEEE Trans. Ultrason. Ferroelectr. Freq. Control 43 (6) (1996) 1122–1129.
[31] J. Antoni, A Bayesian approach to sound source reconstruction: Optimal basis, regularization, and focusing, J. Acoust. Soc. Am. 131 (4) (2012) 2873–2890.
[32] C. Soares, A. Waldhorst, S. Jesus, Matched field processing: environmental focusing and source tracking with application to the North Elba data set, in: Oceans '99. MTS/IEEE. Riding the Crest Into the 21st Century. Conference and Exhibition. Conference Proceedings (IEEE Cat. No.99CH37008), Volume 3, IEEE & Marine Technol. Soc, Seattle, WA, USA, 1999, pp. 1598–1602.
[33] A.P. Mosk, A. Lagendijk, G. Lerosey, M. Fink, Controlling waves in space and time for imaging and focusing in complex media, Nat. Photon. 6 (5) (2012) 283–292.
[34] E.T.F. Rogers, N.I. Zheludev, Optical super-oscillations: sub-wavelength light focusing and super-resolution imaging, J. Opt. 15 (9) (2013) 094008.
[35] J. de Rosny, M. Fink, Overcoming the diffraction limit in wave physics using a time-reversal mirror and a novel acoustic sink, Phys. Rev. Lett. 89 (12) (2002) 124301.
[36] G. Lerosey, J. de Rosny, A. Tourin, M. Fink, Focusing beyond the diffraction limit with far-field time reversal, Science 315 (5815) (2007) 1120–1122.
[37] S.G. Conti, P. Roux, W.A. Kuperman, Near-field time-reversal amplification, J. Acoust. Soc. Am. 121 (6) (2007) 3602.
[38] F. Lemoult, M. Fink, G. Lerosey, Acoustic resonators for Far-Field control of sound on a subwavelength scale, Phys. Rev. Lett. 107 (6) (2011) 064301.
[39] A. Mimani, Z. Prime, C. Doolan, P. Medwell, A sponge-layer damping technique for aeroacoustic time-reversal, J. Sound Vib. 342 (2015) 124–151.
[40] A. Mimani, A point-like enhanced resolution of experimental Aeolian tone using an iterative point-time-reversal-sponge-layer damping technique, Mech. Syst. Signal Process. 151 (2021) 107411.
[41] G.T. Schuster, S. Hanafy, Y. Huang, Theory and feasibility tests for a seismic scanning tunnelling macroscope: Seismic scanning tunnelling macroscope, Geophys. J. Int. 190 (3) (2012) 1593–1606.
[42] B. Guo, Y. Huang, A. Røstad, G. Schuster, Far-field super-resolution imaging of resonant multiples, Sci. Adv. 2 (5) (2016) e1501439.
[43] G. Backus, F. Gilbert, The resolving power of gross earth data, Geophys J Int 16 (2) (1968) 169–205.
[44] J.H. Wilson, Applications of inverse beamforming theory, J. Acoust. Soc. Am. 98 (6) (1995) 3250–3261.
[45] K. Sekihara, M. Sahani, S.S. Nagarajan, Localization bias and spatial resolution of adaptive and non-adaptive spatial filters for MEG source reconstruction, NeuroImage 25 (4) (2005) 1056–1067.
[46] M.-X. Huang, J. Shih, R. Lee, D. Harrington, R. Thoma, M. Weisend, F. Hanlon, K. Paulson, T. Li, K. Martin, G. Miller, J. Canive, Commonalities and differences among vectorized beamformers in electromagnetic source imaging, Brain Topography 16 (3) (2003) 139–158.
[47] B. Van Veen, K. Buckley, Beamforming: a versatile approach to spatial filtering, IEEE ASSP Mag. 5 (2) (1988) 4–24.
[48] Y. Bucris, I. Cohen, M.A. Doron, Bayesian Focusing for coherent wideband beamforming, IEEE Trans. Audio, Speech, Language Proc. 20 (4) (2012) 1282–1296.
[49] M.B. Hawes, W. Liu, Sparse array design for wideband beamforming with reduced complexity in tapped delay-lines, IEEE/ACM Trans. Audio, Speech, Language Proc. 22 (8) (2014) 1236–1247.
[50] M. Rasekh, S.R. Seydnejad, Design of an adaptive wideband beamforming algorithm for conformal arrays, IEEE Commun. Lett. 18 (11) (2014) 1955–1958.
[51] Y. Liu, C. Liu, D. Hu, Y. Zhao, Robust adaptive wideband beamforming based on time frequency distribution, IEEE Trans. Signal Process. 67 (16) (2019) 4370–4382.
[52] W. Liu, S. Weiss, Wideband Beamforming, John Wiley & Sons, Ltd, Chichester, UK, 2010.
[53] B.E. Anderson, J. Douma, T. Ulrich, R. Snieder, Improving spatio-temporal focusing and source reconstruction through deconvolution, Wave Motion 52 (2015) 151–159.
[54] F. Bazargani, R. Snieder, Optimal source imaging in elastic media, Geophys. J. Int. 204 (2) (2016) 1134–1147.
[55] M. Fink, C. Prada, Acoustic time-reversal mirrors, Inverse Problems 17 (1) (2001) R1–R38.
[56] R. Snieder, K.v. Wijk, A Guided Tour of Mathematical Methods for the Physical Sciences, third ed., Cambridge University Press, Cambridge, 2015.
[57] M.V. Berry, S. Popescu, Evolution of quantum superoscillations and optical superresolution without evanescent waves, J. Phys. A: Math. Gen. 39 (22) (2006) 6965–6977.

[58] C. Dolph, A current distribution for broadside arrays which optimizes the relationship between beam width and side-lobe level, Proc. IRE 34 (6) (1946) 335–348.
[59] T. Gallaudet, C. de Moustier, On optimal shading for arrays of irregularly-spaced or noncoplanar elements, IEEE J. Ocean. Eng. 25 (4) (2000) 553–567.
[60] J. Groenenboom, R. Snieder, Attenuation, dispersion, and anisotropy by multiple scattering of transmitted waves through distributions of scatterers, J. Acoust. Soc. Am. 98 (6) (1995) 3482–3492.
[61] L.L. Foldy, The multiple scattering of waves. I. General theory of isotropic scattering by randomly distributed scatterers, Phys. Rev. 67 (3–4) (1945) 107–119.
[62] S. Xiao, S. Altunc, P. Kumar, C.E. Baum, K.H. Schoenbach, A reflector antenna for focusing subnanosecond pulses in the near field, IEEE Antennas Wirel. Propag. Lett. 9 (2010) 12–15.